Chemical Science

ROYAL SOCIETY OF CHEMISTRY

EDGE ARTICLE

View Article Online
View Journal | View Issue

Cite this: *Chem. Sci.*, 2020, **11**, 7910

All publication charges for this article have been paid for by the Royal Society of Chemistry

Multifunctional ionic porous frameworks for CO_2 conversion and combating microbes†

MD. Waseem Hussain, ‡[a] Vipin Bhardwaj, ‡[b] Arkaprabha Giri, [a] Ajit Chande *[b] and Abhijit Patra *[a]

Received 21st March 2020
Accepted 1st July 2020

DOI: 10.1039/d0sc01658f

rsc.li/chemical-science

Porous organic frameworks (POFs) with a heteroatom rich ionic backbone have emerged as advanced materials for catalysis, molecular separation, and antimicrobial applications. The loading of metal ions further enhances Lewis acidity, augmenting the activity associated with such frameworks. Metal-loaded ionic POFs, however, often suffer from physicochemical instability, thereby limiting their scope for diverse applications. Herein, we report the fabrication of triaminoguanidinium-based ionic POFs through Schiff base condensation in a cost-effective and scalable manner. The resultant N-rich ionic frameworks facilitate selective CO_2 uptake and afford high metal (Zn(II): 47.2%) loading capacity. Owing to the ionic guanidinium core and ZnO infused mesoporous frameworks, Zn/POFs showed pronounced catalytic activity in the cycloaddition of CO_2 and epoxides into cyclic organic carbonates under solvent-free conditions with high catalyst recyclability. The synergistic effect of infused ZnO and cationic triaminoguanidinium frameworks in Zn/POFs led to robust antibacterial (Gram-positive, *Staphylococcus aureus* and Gram-negative, *Escherichia coli*) and antiviral activity targeting HIV-1 and VSV-G enveloped lentiviral particles. We thus present triaminoguanidinium-based POFs and Zn/POFs as a new class of multifunctional materials for environmental remediation and biomedical applications.

Introduction

The scientific community is engaged in developing advanced materials for addressing some of the major challenges of the 21st century. Challenges like a steady increase of the CO_2 concentration in the atmosphere with rapid urbanization and its consequence in terms of global warming and climate change are at the forefront and require urgent attention.[1] In addition to this, the growing mortality due to antimicrobial resistance poses a formidable threat to mankind.[2] One of the emerging and worthy areas of materials science research for addressing some of these major concerns is the identification of materials possessing multifunctional properties. Such multifunctional materials – if generated – can serve to tackle today's environmental and biomedical challenges, provided the economic viability is duly considered.[3,4]

Selective CO_2 adsorption and conversion to counteract its increased atmospheric concentration are now being tackled by employing porous materials, starting from porous carbons, zeolites, and metal–organic frameworks (MOFs).[5] In this context, the catalytic fixation of CO_2 with epoxides into cyclic organic carbonates has drawn considerable interest due to the high atom economy of the reaction and the extensive commercial use of materials derived from cyclic carbonates.[6] Heteroatom-rich, hierarchically porous organic polymers (POPs), having synthetic flexibility and easy post-synthetic modification along with high thermal and hydrothermal stability, have emerged as a promising heterogeneous platform for catalytic conversion of CO_2.[3a,7,8] N-Rich ionic porous organic frameworks (POFs), a subclass of POPs having a certain degree of ordered network,[9] promote the catalytic conversion of CO_2 due to the exchangeable counter ions acting as nucleophiles for epoxide ring-opening.[10] At the same time, similar to antimicrobial peptides (AMPs), ionic POFs can disrupt the growth of microbes through electrostatic interactions with their charged membranes.[2a,11] Recently, Banerjee and coworkers employed triaminoguanidinium-based ionic frameworks for antibacterial applications.[12] Zhu and coworkers reported pyridinium-based porous aromatic frameworks and their AgCl-loaded counterparts as effective antimicrobial coatings.[2c] The incorporation of metal coordination in the porous frameworks provides additional Lewis-acidic sites that may enhance both the catalytic conversion of CO_2 and antimicrobial activity.[2c,13]

[a]*Department of Chemistry, Indian Institute of Science Education and Research Bhopal, Bhopal Bypass Road, Bhauri, Bhopal 462066, Madhya Pradesh, India. E-mail: abhijit@iiserb.ac.in*

[b]*Department of Biological Sciences, Indian Institute of Science Education and Research Bhopal, Bhopal Bypass Road, Bhauri, Bhopal 462066, Madhya Pradesh, India. E-mail: ajitg@iiserb.ac.in*

† Electronic supplementary information (ESI) available: Details of synthesis and characterization, catalytic CO_2 conversion, antibacterial and antiviral studies, and comparative analysis of multifunctional properties and applications. CCDC 1966910. For ESI and crystallographic data in CIF or other electronic format see DOI: 10.1039/d0sc01658f

‡ Equal contribution.

In the quest for multifunctional materials for CO_2 conversion and effective antimicrobial action, we developed triaminoguanidinium-based ionic porous frameworks (POFs) through Schiff base condensation. N-Rich ionic frameworks enable chelation with Zn(II) in the form of ZnO. The high loading of ZnO, resulting in Zn/POFs, remarkably enhances the catalytic as well as antimicrobial activity (Tables S5–S8, ESI†). Zn/POFs are reusable for multiple cycles, retaining high catalytic activity. Investigations on bacterial growth dynamics, cell viability, and lysis, evidenced using transmission electron microscopy and fluorescence imaging with Gram-positive bacteria, Gram-negative bacteria, and viral strains with distinct entry mechanisms including human immunodeficiency virus-1 (HIV-1), unequivocally establish Zn/POFs as robust antimicrobial agents. The catalytic CO_2 conversion and antimicrobial action, including the first-time demonstration of antiviral activity by porous framework materials, pave the way for the development of multifunctional materials addressing global issues of environmental protection and antimicrobial resistance.

Results and discussion

Synthesis and characterization of the POFs and Zn/POFs

The emerging arena of ionic POFs for catalysis and antibacterial activity[10c,12,14] motivated us to use the triaminoguanidinium (TAG; Scheme S1 and Fig. S1, ESI†) cation as a triangular building block for the development of ionic nanoporous frameworks. The N-rich guanidinium core is known for its antibacterial activity and suitable for anchoring metal ions.[11c,15] The incorporation of a Lewis acidic metal centre into the POF is likely to enhance the catalytic activity and imparts specific interactions with microbial membranes. In this context, the immobilization of low-cost zinc oxide (ZnO) having antimicrobial activity into the framework can be a viable option. However, aggregation of ZnO particles may diminish the activity. In addition, the dose at which ZnO exerts an antimicrobial action is toxic to eukaryotic cells.[16] Hence, the development of a recyclable material with superior activity as well as low toxicity is a challenge. We envisioned that the ZnO-loaded ionic network involving TAG might lead to multifunctional materials for heterogeneous catalysis and combating microbes with superior activity as well as low cytotoxicity to mammalian cells. So, we set out to fabricate ionic POFs *via* Schiff base polycondensation reaction between triaminoguanidinium chloride (TAG-Cl) and terephthalaldehyde (A3 + B2 polycondensation: POF1), and benzene-1,3,5-tricarboxaldehyde (A3 + B3 polycondensation: POF2) (Fig. 1a and Scheme S2, ESI†). The metalation of pristine frameworks (POF1 and POF2) was carried out by refluxing with 10 wt% $Zn(OAc)_2$ in EtOH. The fabrication method is highly scalable and does not require any costly catalysts. The POFs and the corresponding Zn/POFs were purified through Soxhlet extractions using MeOH and $CHCl_3$ each for 24 h. The mechanistic investigation supported by earlier literature reports suggests that triaminoguanidinium-based POFs act as the catalyst as well as the template for the unprecedented *in situ* formation of ZnO from the precursor $Zn(OAc)_2 \cdot 2H_2O$ (Fig. S9–S11, ESI†).[17]

The Fourier transform infrared spectroscopy (FTIR) analysis of POFs revealed a C=N stretching at 1632 cm^{-1}, indicating the cross-condensation between the monomers (Fig. 1b, S3 and S4, ESI†). The peak at 1102 cm^{-1} is assignable to the C–N stretching of the TAG unit. The new peak at 462 cm^{-1} (Zn–O stretching) in Zn/POFs is attributed to the formation of ZnO (Fig. 1b and S5, ESI†). The shift of the peak at 1632 cm^{-1} in POFs to 1566 cm^{-1} in Zn/POFs indicates the increase of C=N bond length due to the ZnO loading, further indicating the metal coordination in the polymer framework. The solid-state ^{13}C cross-polarization magic angle spinning (CP/MAS) NMR spectra of POFs showed a peak resonating at 198 ppm due to the imine carbon atom, suggesting cross-condensation between the monomeric units (Fig. S41, ESI†).

The thermogravimetric analysis (TGA) profiles of POFs demonstrate high thermal stability up to ~250 °C (Fig. 1c, S6 and S7, ESI†). The weight residue of POF2 at around 900 °C is 21.2 ± 0.5% compared to 78.5 ± 1.7% for Zn/POF2, suggesting 57.3 ± 1.2% loading of ZnO in Zn/POF2 (Fig. 1c). The powder X-ray diffraction (PXRD) analysis of the POFs showed a broad peak at $2\theta \sim 26.0°$ and a hump at ~10.3° (Fig. 1d and S8, ESI†). The low crystallinity of TAG-based POFs is likely to be due to the electrostatic repulsion between the two layers of cationic triaminoguanidinium units and intercalated chloride ions leading to poor π–π stacking. The observation is also consistent with previous literature reports.[12,18] Interestingly, the packing of the model compound, MTAG (CCDC no. 1966910, Scheme S3, ESI†), based on TAG-Cl and benzaldehyde, depicts the chloride ions which are sandwiched between successive layers with an interplanar distance of 3.6 Å (Fig. 1e and S2, ESI†). Accordingly, we modelled the framework structure and simulated the PXRD patterns (Fig. 1f and S8, ESI†). Considering the broad PXRD pattern of the framework, it is challenging to unambiguously ascertain the conformation as eclipsed or staggered (Fig. 1f and S8, ESI†). Hence, from the experimental and the simulated PXRD patterns, it is likely that POFs have a mixture of eclipsed and staggered conformations. Well-defined sharp peaks were observed for Zn/POFs (Fig. 1d, and S9 and S10, ESI†) in addition to the broad peak of POFs. The Miller planes (100), (020), (101), (102), and (110) suggest the presence of ZnO in the würtzite form (JCPDS 36-1451).[19] No peaks of $Zn(OAc)_2$ were obtained in Zn/POFs (Fig. S9 and S10, ESI†). Thus, PXRD analysis, coupled with FTIR and TGA, unambiguously ascertain the immobilization of ZnO in Zn/POFs (Fig. S11, ESI†).

The field emission scanning electron microscopy (FESEM) images of POF1 and POF2 show a network-like and a granular morphology, respectively (Fig. 1g, S12a and S13a, ESI†). In contrast, agglomerated structures are noticeable in the case of Zn/POF1 and Zn/POF2 (Fig. 1h, and S12b and S13b, ESI†). The transmission electron microscopy (TEM) images of POF2 and Zn/POF2 also revealed the porous nature of the frameworks (Fig. 1g and h, inset; Fig. S14, ESI†). The high-angle annular dark-field (HAADF) imaging of Zn/POF2 indicates the homogeneous distribution of ZnO in the framework (Fig. S16, ESI†). The N1s X-ray photoelectron spectroscopy (XPS) results showed a single peak at 398.01 eV for Zn/POF2 compared to the binding energy at 398.44 eV for pristine POF2 (Fig. S17b and S18b†). The

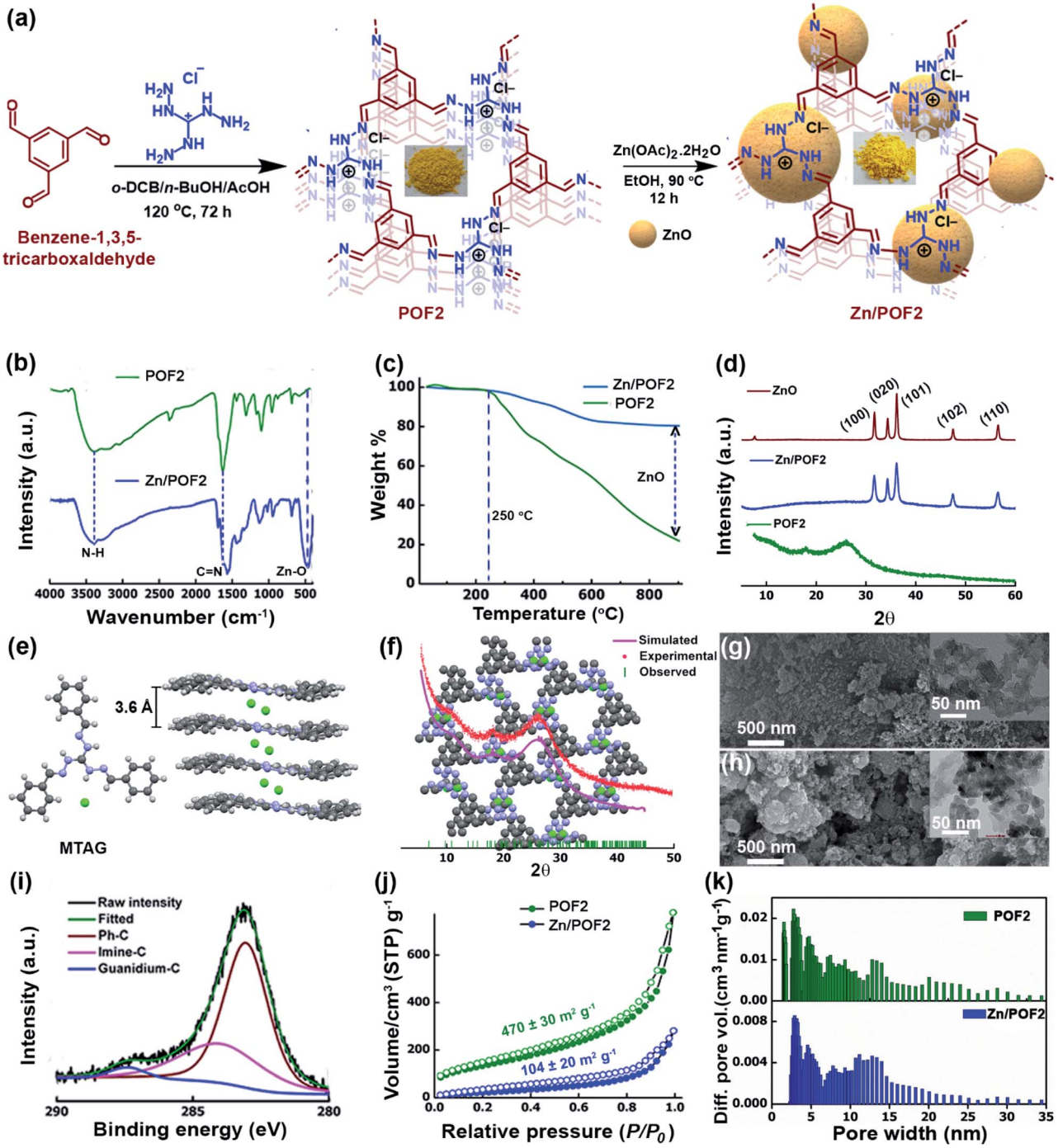

Fig. 1 (a) Synthetic schemes of the triaminoguanidinium-based ionic porous organic framework (POF2) and ZnO-loaded framework (Zn/POF2, the crystallite/particle size of ZnO is not to scale as per the pore sizes of the frameworks in the pictorial depiction). (b) The Fourier transform infrared (FTIR) spectra of POF2 and Zn/POF2. (c) The thermogravimetric analysis (TGA) of POF2 (green) and Zn/POF2 (blue) demonstrating the high loading of ZnO in Zn/POF2. (d) The comparative analysis of the powder X-ray diffraction pattern of POF2, Zn/POF2, and ZnO illustrating the loading of ZnO in Zn/POF2. (e) The crystal structure and packing of the model compound based on triaminoguanidinium chloride and benzaldehyde (MTAG) depicting Cl^- ions sandwiched between the layers. (f) The PXRD analysis of POF2: simulated PXRD pattern (pink), experimental PXRD pattern (red), observed peaks (green) and the eclipsed structure model of POF2 (top view); grey: carbon, blue: nitrogen, green: chlorine. The FESEM and TEM (inset) images of (g) POF2 and (h) Zn/POF2, respectively. (i) The C1s XPS analysis of Zn/POF2. (j) The nitrogen sorption isotherms of POF2 (green) and Zn/POF2 (blue) measured at 77 K; solid circles represent adsorption, and open circles represent desorption. (k) The pore size distribution estimated by the non-local density functional theory (NLDFT) method depicting hierarchical porosity in POF2 and Zn/POF2.

C1s XPS analysis of POFs and Zn/POFs demonstrates the presence of phenylic-C (POF2: 282.8 eV, Zn/POF2: 283.1 eV), guanidinium-C (POF2: 286.6 eV, Zn/POF2: 287.1 eV), and imine-C (POF2: 284.0 eV, Zn/POF2: 283.9 eV; Fig. 1i, and S17–S19, ESI†). The percentage Zn(II) loading was found to be 47.2 wt% for Zn/POF2 as obtained from the XPS analysis, consistent with the TGA data (Table S2, ESI†). The inductively coupled plasma-optical emission spectrometry (ICP-OES) analysis of Zn/POF2 also corroborates the values obtained from the XPS analysis (Tables S2 and S4,† ESI).

The porosity and the surface area of the POFs were estimated using nitrogen gas sorption analysis at 77 K (Fig. 1j, and S20 and S21, ESI†). POFs exhibit type II sorption isotherms (Fig. 1j and S20, ESI†), indicative of mesoporous characteristics.[20] The Brunauer–Emmett–Teller (BET) specific surface area of POF1 and POF2 was found to be 200 ± 20 and 470 ± 30 $m^2\ g^{-1}$ with a total pore volume of 0.30 and 0.22 $cm^3\ g^{-1}$, respectively, at $P/P_0 = 0.9$. Upon ZnO loading, the specific BET surface area was decreased; it was found to be 40 ± 5 and 104 ± 20 $m^2\ g^{-1}$ for Zn/POF1 and Zn/POF2, respectively (Fig. 1j and S21, ESI†). The pore size distribution analysis revealed pore dimensions ranging from 1.5 to 20 nm both for POF2 and Zn/POF2 (Fig. 1k). Such hierarchical pore size distribution in the microporous as well as mesoporous regime facilitates mass transfer and is suitable for catalytic applications.[3a] The decrease in the specific BET surface area of Zn/POF2 from that of POF2 and shifting of the pore size distribution from the microporous to the narrow mesoporous region suggest immobilization of ZnO particles throughout the surface as well as in the interlayer spaces of the host framework. The CO_2 uptake by POF2 and Zn/POF2 was 7.4 and 6.2 wt%, respectively, at 273 K and 1 bar (Fig. S22a and S24a, ESI†). The isosteric heat of adsorption (Q_{st}) value of pristine POF2 was 20.6 kJ mol^{-1} (CO_2/N_2 selectivity: 48, Fig. S22b and S25, ESI†). The strong dipole–quadrupole interaction between the N-rich triaminoguanidinium core and CO_2 leads to the high Q_{st} value.[21]

CO_2 conversion

The high affinity of POFs and Zn/POFs with CO_2 prompted us to investigate the catalytic performance of the frameworks in the conversion of CO_2 and epoxides into cyclic carbonates. The multifarious applications of cyclic organic carbonates such as polar aprotic solvents, fuel additives, electrolytes for Li-ion batteries and polycarbonate precursors place the cycloaddition of CO_2 and epoxides as an industrially relevant reaction.[6] The reaction was carried out using porous frameworks (POFs as well as Zn/POFs) as the catalyst, and tetra-*n*-butylammonium bromide (TBAB, 2.5 mol%) as the cocatalyst under the optimized reaction conditions of 90 °C and 2.5 bar pressure of CO_2 (Fig. 2a and Table S3, ESI†). Without the cocatalyst, the catalyst (POFs as well as Zn/POFs) afforded a very low conversion of <2% (Table S3†). In contrast, ~17% cyclic carbonate was obtained using only the cocatalyst (TBAB) (Table S3†). POFs and Zn/POFs achieved ~46 to 51% and 92–94% conversion to propylene carbonate, respectively, with TBAB (2.5 mol%, Table S3†). The high catalytic efficiency of Zn/POFs compared to that of the pristine POFs suggests the importance of the Lewis acidic metal centres for the activation of epoxides in addition to N-rich CO_2-philic ionic frameworks (Fig. S26, ESI†).

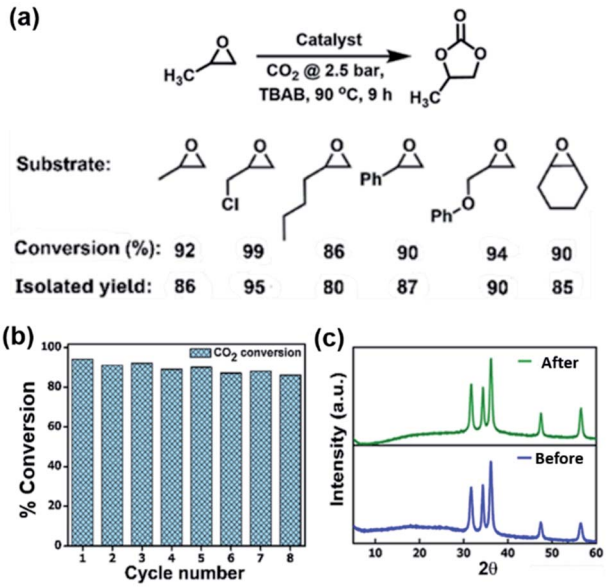

Fig. 2 (a) Catalytic performance of ionic POFs and Zn/POFs in the cycloaddition of CO_2 and propylene oxide: the substrate scope, percentage of conversion, and isolated yields are indicated. Epoxide (17.2 mmol), TBAB (cocatalyst, 2.5 mol%, 0.43 mmol), catalyst (POF or Zn/POF: 2 wt%, 20 mg), CO_2 (2.5 bar), 90 °C and 9 h. The substrate scope was explored employing Zn/POF2 (20 mg) as the catalyst. % of conversion was determined by the ^{1}H NMR analysis of the reaction mixture with 1,1,2,2-tetrachloroethane as an external standard. (b) Recyclability of Zn/POF2 after catalytic cycloaddition reaction between propylene oxide and CO_2 by maintaining a fixed amount of catalyst of 20 mg, circumventing the weight loss (1–1.5 mg per cycle) during the recovery process; more than 90% conversion for multiple cycles ascertain no loss in catalytic efficiency. (c) The PXRD profiles of the pristine and regenerated catalysts demonstrating the robustness of Zn/POF2 in catalytic CO_2 conversion.

A plausible mechanism for the conversion of epoxide to the corresponding cyclic carbonates involves the activation of epoxide by the pristine frameworks through H-bonding interactions (Fig. S26, ESI†).[6b,7a,22] The process is further facilitated by Lewis acidic Zn(II) centers in Zn/POFs. The broad applicability of the catalyst (Zn/POF2) in the conversion of substituted epoxides to their corresponding cyclic organic carbonates is shown in Fig. 2a (Table S3, ESI†); the high percentage of conversion is noticeable for varieties of substrates. Moreover, Zn/POF2 showed excellent recyclability. More than 90% conversion was observed even after eight cycles (circumventing the weight loss of 1–1.5 mg in each cycle, Fig. 2b and S27, ESI†). The chemical stability of the recovered Zn/POF2 after multiple cycles of use was ascertained through PXRD (Fig. 2c), FTIR (Fig. S27b, ESI†), and morphological analysis (Fig. 1h and S27c, ESI†). The hot-filtration test followed by TGA suggested no significant weight loss due to the metal-leaching (Fig. S7, ESI†). The ICP-OES analysis of Zn/POF2 after multiple cycles of catalysis indicated less than 2% loss of ZnO, signifying the robustness of the catalyst (Table S4†). Thus, ZnO-impregnated

triaminoguanidinium-based ionic porous organic frameworks are promising for heterogeneous catalytic fixation of CO_2 under solvent-free reaction conditions (Table S6†).

Antibacterial activity

The ionic frameworks with a guanidinium core and high loading of ZnO encouraged us to explore the ability of the materials to affect the microbial growth. To this end, we performed the growth curve analysis with and without the porous framework using representative strains of Gram-positive (*Staphylococcus aureus*) and Gram-negative (*Escherichia coli*) bacteria (Fig. 3). The bacterial growth dynamics for both *E. coli* and *S. aureus* were carried out in a 24 well plate format with 10^5 CFU mL^{-1} in LB (Luria–Bertani) broth with increasing doses (100, 200 and 500 μg mL^{-1}) of the porous frameworks. The working concentration used in this study is consistent with the previously reported antimicrobial studies employing porous organic frameworks and ZnO-based materials.[12,23] The growth was monitored in a real-time manner, and the values obtained were plotted, considering the absorbance at 600 nm *versus* the incubation time.[24] The relatively slower growth rate of *S. aureus* against POF2 compared to that of *E. coli* suggests the more effective interaction of the cationic framework with the former (Fig. 3a and e). It can be due to the presence of loosely packed glycan chains in the peptidoglycan lattice in the case of *S. aureus*, unlike *E. coli*, with an additional bilayer phospholipid structure.[2a] The sluggish growth dynamics of *S. aureus* compared to that of *E. coli* in the presence of Zn/POF2 further implies stronger interactions with the former (Fig. 3b and f). The relatively higher activity of Zn/POF2 compared to that of POF2 is plausibly due to the synergistic effect of ZnO and the cationic triaminoguanidinium framework. This observation is also consistent with the percentage viability plots (Fig. 3c and

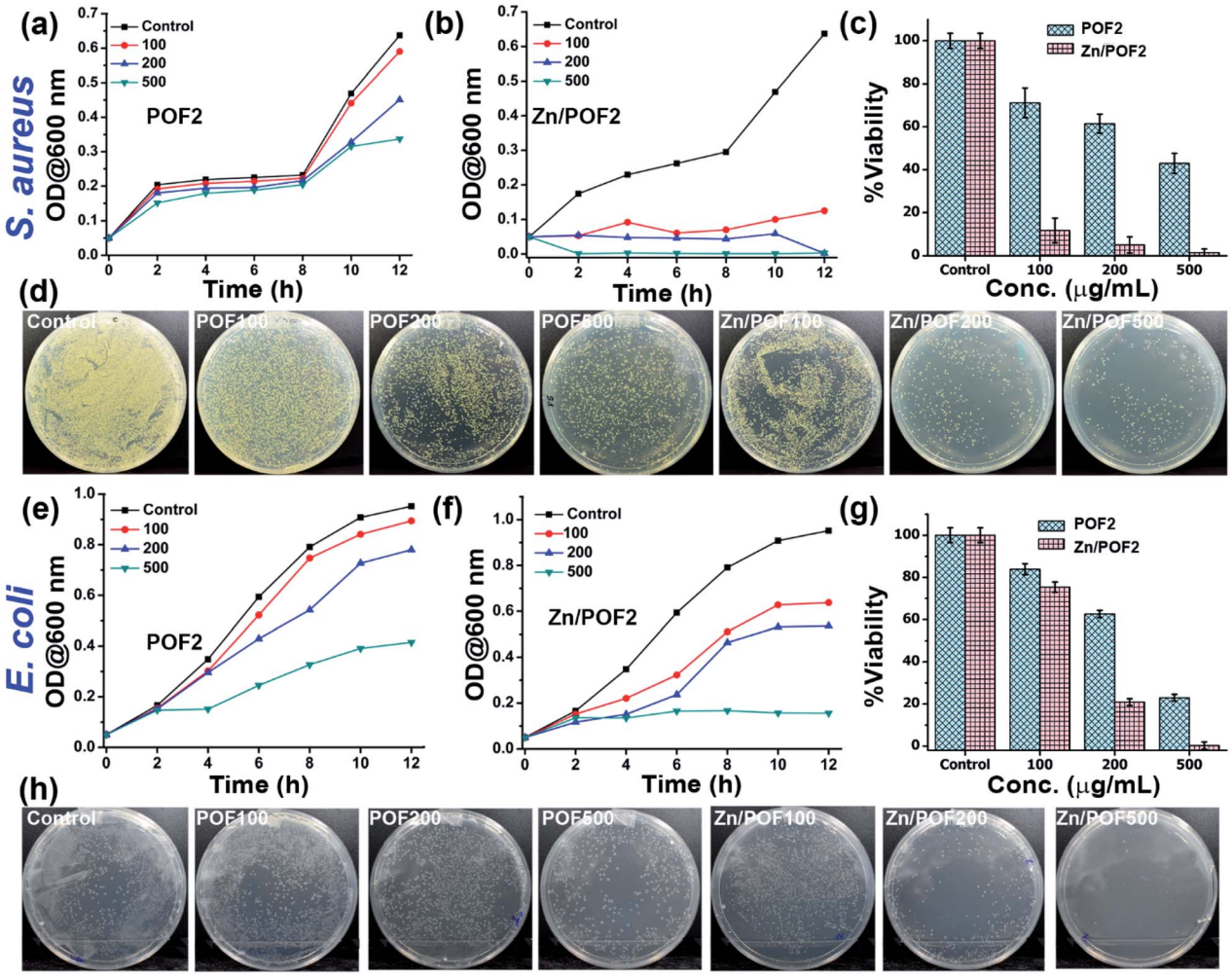

Fig. 3 Antibacterial activity analysis of POF2 and Zn/POF2 by real-time growth curve analysis and systematic colony-forming unit (CFU) imaging. Action against Gram-positive bacteria (*Staphylococcus aureus*): growth curves of (a) POF2 and (b) Zn/POF2, (c) percentage viability with increasing concentration of POF2 and Zn/POF2, and (d) comparative CFU images with increasing concentration of POF2 and Zn/POF2 (100, 200, and 500 μg mL^{-1}) with respect to the control. Action against Gram-negative bacteria (*Escherichia coli*): growth curves of (e) POF2 and (f) Zn/POF2, (g) percentage viability with increasing concentration of POF2 and Zn/POF2, and (h) comparative CFU images with increasing concentration of POF2 and Zn/POF2 (100, 200, and 500 μg mL^{-1}) with respect to the control. The error bars represent the standard deviation from the mean ($n = 3$, mean ± sd).

g). The alamarBlue assay against *E. coli*, performed in the presence of various doses (50, 100, 200, 300, and 500 μg mL^{-1}) of Zn/POF2 (Fig. S29, ESI†), indicates reduced cellular viability consistent with the inadequate reduction of resazurin to a strongly fluorescent resorufin in the presence of porous frameworks (Fig. S30, ESI†).[25]

Furthermore, the bacterial cell-viability assays against both *S. aureus* and *E. coli* with different concentrations of POF2 and Zn/POF2 were visualized by a classical agar plating method. The respective bacterial suspensions with POF2 or Zn/POF2 were incubated for 12 h at 37 °C, and the live cells were taken from the suspension and allowed to grow on agar plates overnight at 37 °C for the assessment of the colony-forming units (CFUs). The suspension without POF2 or Zn/POF2 served as a control. The results of photographic representation over the agar plate are shown in Fig. 3d and h, as CFUs relative to increasing concentrations (100–500 μg mL^{-1}) of POF2 and Zn/POF2 with respect to the control. As a function of bacterial cell growth, the CFUs for Gram-positive and Gram-negative bacteria showed a concentration-dependent reduction of the bacterial colonies, indicating the high antibacterial activity of both POF2 and Zn/POF2 (Fig. 3d and h). Zn/POF2 exhibited strong activity against both the bacteria (*S. aureus* and *E. coli*), demonstrating that the infusion of ZnO in Zn/POF2 enhanced the antibacterial activity.[2b,16b] We further investigated the antibacterial action of the porous frameworks (POFs and Zn/POFs) using transmission electron microscopy (TEM) imaging. The untreated (control) and post-treated bacterial samples with the porous frameworks (POFs as well as Zn/POFs) were first fixed using glutaraldehyde prior to imaging (Fig. 4). The untreated *S. aureus* was observed to have a sphere-like morphology with intact cell membranes (Fig. 4a and b), while the bacteria treated with POF2 (Fig. S31a and S31b, ESI†) and Zn/POF2 (Fig. 4e and f) showed the presence of ruptured cell morphology as evident from the TEM imaging. Similar observations were also made in the case of *E. coli* where the untreated bacterial sample showed a regular rod-like structure (Fig. 4c and d).[12,26] The treatment with POF2 (Fig. S31c and d, ESI†) and Zn/POF2 (Fig. 4g and h) revealed a shrunken and skewed morphology indicating the possible rupture of cells.

Biofilm formation on maritime transport, oil industries, desalination plants, medical devices, *etc.* leads to corrosion, biofouling, and infected surfaces.[27] Hence, the fabrication of smart antibacterial surfaces has attracted a great deal of interest.[2c,28] Recently, Wang and coworkers reviewed various strategies and materials developed for effective biofilm disruption.[28c] Interestingly, the antibacterial activity of POFs as well Zn/POFs was not limited to liquid bacterial culture but was even applicable to the disruption of the biofilm formed by *E. coli* (Fig. 5a and b, and S32, ESI†). We observed a moderate performance for pristine POF2, while Zn/POF2 showed considerable biofilm disruption (Table S8, ESI†). The biofilm disruption ability of Zn/POF2 prompted us to further fabricate the antibacterial surface by embedding Zn/POF2 in poly(vinylalcohol) thin film (Fig. S33, ESI†).

To further explore the effect of porous frameworks (POFs and Zn/POFs) on the bacterial cells (*E. coli*), we performed the 'live/dead' cell staining using a mixture of SYBR Green I and propidium iodide (PI) dyes (Fig. 5c).[29] Briefly, the treated bacterial cells were incubated with the dye mixture (SYBR Green I and PI). SYBR Green-I can diffuse through the lipid membrane of both the live as well as the dead bacteria, while PI specifically enters

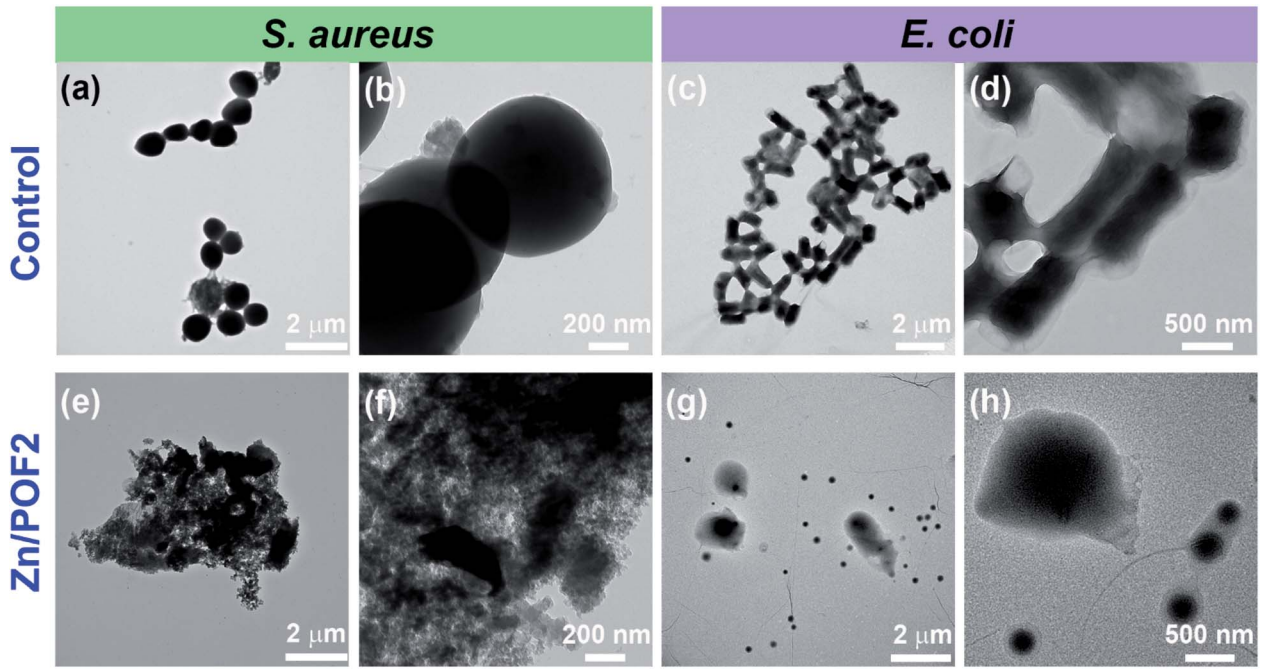

Fig. 4 Analysis of cell integrity upon treatment of POF2 and Zn/POF2 using transmission electron microscopy (TEM). Gram-positive bacteria (*S. aureus*): (a and b) control, and after treatment with (e and f) Zn/POF2. Gram-negative bacteria (*E. coli*): (c and d) control, and after treatment with (g and h) Zn/POF2.

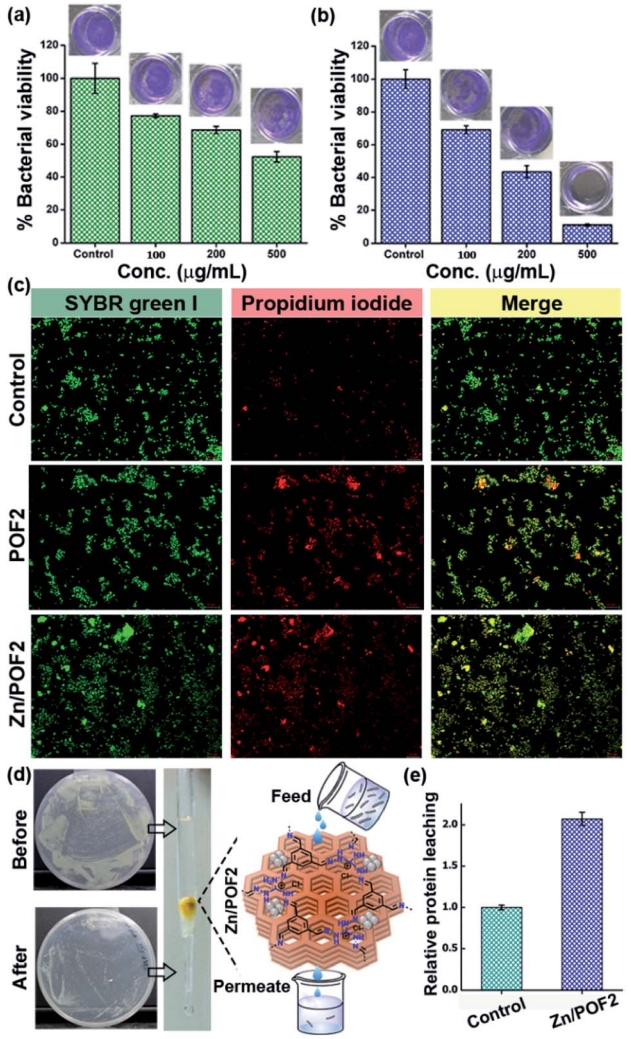

Fig. 5 The *E. coli* biofilm disruption due to various concentrations (μg mL^{-1}) of (a) POF2 and (b) Zn/POF2. (c) Live/dead bacterial cell imaging using a dye mixture of SYBR Green I and propidium iodide staining of untreated (control), POF2, and Zn/POF2-treated *E. coli* cells. (d) The clearance of bacteria-contaminated water (*E. coli* ~10^8 CFU mL^{-1}) by passing through a column packed with the porous framework, Zn/POF2, evidenced by the CFU plating studies. (e) The relative protein leaching in the column flow-through using the Bradford assay, suggesting bacterial lysis after passing through the column of Zn/POF2. The *Y*-axis values were normalized to the eluted fraction obtained from the agarose-packed control column.

when membrane integrity is compromised as is the case with dead bacterial cells. A plausible mechanism depicting the antibacterial activity of POFs as well as Zn/POFs is demonstrated in Fig. S34, ESI.† The pristine POFs containing a positively charged guanidinium backbone possibly interact with the negatively charged lipid membrane of the bacterial cell-wall and rupture the bacterial cells exhibiting moderate antibacterial activity.[30] In comparison, Zn/POFs with additional Lewis-acidic metal sites show enhanced bactericidal activity.[2b]

Disinfection of water has drawn a great deal of attention due to the worldwide shortage of potable water. From this perspective, we employed the Zn/POF matrix for clearing bacterial load from the water sample through gravimetric column filtration (Fig. 5d and e, and S35–S37, ESI†). Reduction in the CFU (Fig. 5d and S35, ESI†) coupled with the analysis of the clearance of bacteria by live/dead cell imaging (Fig. S36, ESI†), agarose gel analysis of the released DNA (Fig. S37, ESI†), and the leaching of protein estimated with Bradford assay (Fig. 5e) in the presence of Zn/POF2 in the flow-through suggest a promising application for disinfection of water by clearing the live bacterial load.

Antiviral action

Apart from the antibacterial activity of the porous framework, owing to the presence of the guanidinium functional group, we further anticipated the antiviral activity for POFs as well as Zn/POFs. For confirmation, we evaluated antiviral activities in the TZM-GFP cell line against single-cycle HIV-1 and vesicular stomatitis virus glycoprotein (VSV-G) pseudotyped GFP-encoded lentiviral vectors (LV VSV-G).[31] The virus was produced from human embryonic kidney (HEK293T) cells by co-transfecting helper plasmids.[32] The virus-containing supernatant was added to the TZM-GFP cell line (as target cells) pre-incubated for 4 h with different doses of POF2 and Zn/POF2 (Section V, ESI†). Virus infectivity was calculated after counting the fluorescent green cells as a function of successful virus entry. As shown in Fig. 6a and b (Fig. S38, ESI†), Zn/POF2 showed enhanced antiviral activity against both HIV-1 and VSV-G pseudoparticles plausibly due to the synergistic effect of ZnO and the triaminoguanidinium framework. In contrast, a relatively lower inhibition of viral infectivity was observed with POF2 because of the presence of the triaminoguanidinium framework only.[15a] Interestingly, the effective doses of POFs and Zn/POFs were found to be non-toxic to the human cells used in viral infectivity assay. However, an equivalent amount of free ZnO powder, as well as ZnO nanoparticles, in comparison to Zn/POF2, is toxic to the target cells (Fig. S39, ESI†).

High-content imaging analysis of infected cells revealed reduced infected cell counts upon the use of POF2 or Zn/POF2 at an effective concentration of 20 μg mL^{-1}, suggestive of an antiviral action that plausibly targets an early step in virus infection. It is noteworthy that the amount used for the study is comparable to or lower than those in previous reports with ZnO-based materials.[23] The action of Zn/POF on the virus life cycle was therefore tested next to gain mechanistic insights into the framework action. To this end, we employed an assay that reports viral-mediated delivery of a Cre recombinase protein into the target cells as a function of virus fusion.[31] Upon delivery of Cre recombinase, the protein traverses the cytoplasm to reach the nucleus where it translationally activates a nuclear red fluorescent protein (RFP) reporter by recombining the loxP sites. This assay, therefore, reliably measures the early stages of the virus infection to the target cells. Treatment of the target cells (TZM-Lox-RFP) in the presence of porous frameworks (POF2 and Zn/POF2) revealed a potent activity of Zn/POF2 to restrain the virus early by targeting the fusion step with target cells (Fig. 6c and d). As shown in Fig. 6c, the inhibition of fusion as measured by the number of RFP positive cells, however, was

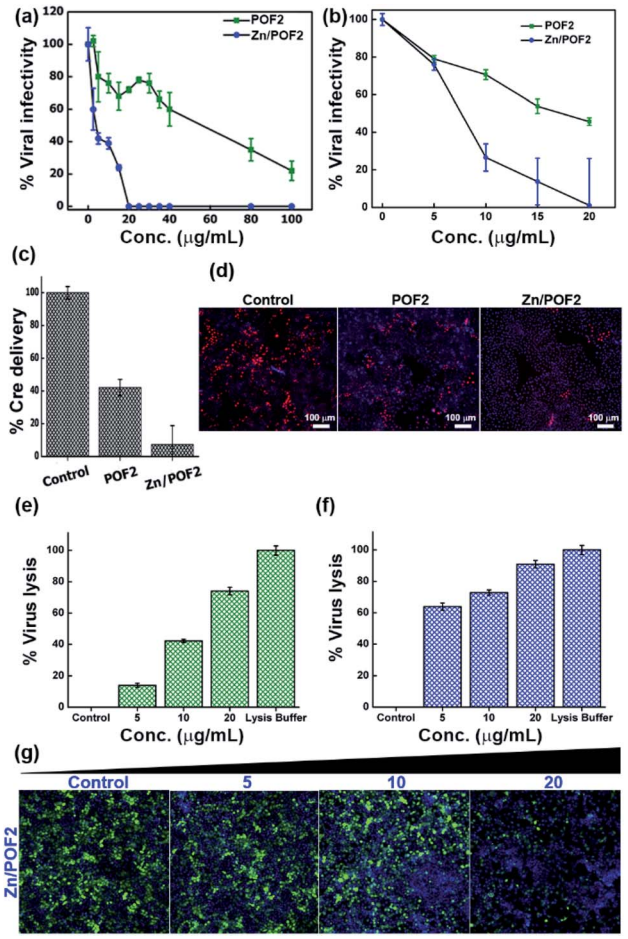

Fig. 6 The single cycle (a) human immunodeficiency virus-1 (HIV-1) and (b) vesicular stomatitis virus glycoprotein (VSV-G)-pseudotyped lentiviral vector infectivity in TZM-GFP target cells scored using a high-content screening platform and expressed in percentage with respect to the control; POF2 (green) and Zn/POF2 (blue). (c) The fusion assay of VSV-G lentiviral pseudoparticles against the porous frameworks POF2 and Zn/POF2 (20 μg mL^{-1}). The error bars represent the standard deviation from the mean ($n = 4$, mean ± sd). (d) The representative images of Cre delivery as a function of fusion with the porous frameworks, POF2 and Zn/POF2 (20 μg mL^{-1}), demonstrating the lower number of red fluorescent protein (RFP) positive cells in the case of Zn/POF2 than POF2 than control. The virus (VSV-G) lysis assay experiment showing the percentage of virus lysis in comparison with the lysis buffer against (e) POF2 and (f) Zn/POF2 with varying concentrations ($n = 4$, mean ± sd). (g) The assay demonstrating the loss of infectivity concomitant with virus lysis with the increasing dose (μg mL^{-1}) of Zn/POF2; green cells represent the viral infected cell population, and Hoechst stained blue cells represent the total cell population.

modest in the case of POFs. The antiviral action of porous frameworks (POFs and Zn/POFs) can be due to the electrostatic interaction between the negatively charged lipid membrane and the positively charged porous frameworks that disrupts virion membrane integrity to inhibit an early stage of virus infection (Fig. S40, ESI†). If this is the standing hypothesis, the rupture of the lipid-containing virus envelope would result in the release of viral content, including its enzyme, the reverse transcriptase (RT). To test this possibility, we performed two different virucidal assays to check the lytic potential of POF2 and Zn/POF2. The first assay was based on the release of RT upon virus lysis. The quantum of released RT was measured using SGPERT (SYBR Green I-based product-enhanced RT) assay performed using a real-time PCR (RT PCR).[33] The quantitative C_t (cycle threshold) values from RT PCR are represented as relative percentage virus lysis indicative of released RT in the supernatant upon treatment with POF2 and Zn/POF2 due to particle lysis (Fig. 6e and f, and S40, ESI†).[34]

To further ascertain the mechanism of the antiviral activity of the porous frameworks, we adopted the second virucidal assay to complement the RT release assay according to the standard protocol with slight modifications.[35] Precisely, we incubated the virus along with the various doses (5, 10, and 20 μg mL^{-1}) of Zn/POF2 (Fig. 6g). After incubation, instead of diluting, the virus-containing frameworks were removed by centrifugation, and the supernatant having viruses was added to the TZM-GFP cell line (reporter cell line). The reduced virus infectivity showed the virucidal activity of the porous framework (Fig. 6g). The lack of recovery of the virus infectivity upon removal of the frameworks further ascertains the virucidal effect over virustatic.[36] The presence of the guanidinium core in the porous frameworks, as well as infused ZnO in Zn/POFs, thus determines the broad antimicrobial activity, including bactericidal and virucidal efficacy.

Conclusions

In summary, we developed triaminoguanidinium-based ionic POFs employing a scalable protocol using Schiff base condensations. The N-rich frameworks facilitated high loading of ZnO through coordination. Both the POFs as well as ZnO-rich Zn/POFs showed the catalytic conversion of CO_2 and epoxides into cyclic organic carbonates under solvent-free reaction conditions. Remarkably, more than 90% conversion of a range of substituted epoxides to the corresponding cyclic carbonates was obtained employing Zn/POFs, reusable for multiple cycles. Zn/POFs also exhibited robust antibacterial and antiviral activity due to the synergistic effect of the immobilized ZnO and guanidinium-based ionic framework. An investigation comprising complementary assays coupled with electron and optical fluorescence microscopy imaging confirmed Zn/POFs as broad-spectrum antimicrobial agents. Such multifunctional applications of Zn/POFs ranging from catalysis to combating microbes as diverse as bacteria and viruses, to the best of our knowledge, are unique in the field of porous materials (Tables S6 and S7†). Crucial observations, including the bactericidal effect promising for water purification and the antiviral action delineated in the current study, open the door for a range of biomedical and environmental applications of porous ionic frameworks in addition to CO_2 conversion to value-added chemicals.

Experimental section

Synthesis

The triaminoguanidinium chloride was synthesized using guanidine hydrochloride following a reported procedure

(Scheme S1, ESI†).[37] The POFs (POF1 and POF2) were fabricated *via* a Schiff base polycondensation reaction between TAG (0.31 mmol) and 1,3,5-benzenetricarboxaldehyde (0.31 mmol) or terephthalaldehyde (0.53 mmol) in a Schlenk tube using *o*-dichlorobenzene, *n*-butanol, and acetic acid in a ratio of 5 : 5 : 1 mL, respectively (Fig. 1a). The reaction mixture was degassed under liquid N_2 (77 K) three times by successive freeze–pump–thaw cycles and stirred at 120 °C for 3 days in an inert atmosphere of N_2. The yellow-colored solids were filtered and purified *via* extensive Soxhlet extractions with methanol, acetone, and chloroform each for 24 h, respectively. Furthermore, refluxing the POFs with $Zn(OAc)_2$ (10 wt% in EtOH) led to the ZnO-infused porous frameworks (Zn/POFs, Fig. 1a, Scheme S2†).

Antimicrobial studies

The antibacterial studies were performed on *Staphylococcus aureus* (*S. aureus*) and *Escherichia coli* (*E. coli*) obtained from Himedia. Both the bacterial strains were grown in Luria–Bertani (LB) medium (DIFCO) cultured aerobically at 37 °C in a glass culture tube with shaking at 200 rpm in a shaker incubator (Infors HT). In order to investigate the antimicrobial activity of nanoporous frameworks, we used optical density and plating assay as a measure of bacterial growth and viability.[38]

For the antiviral studies, single cycle Env-defective and nef-defective NL4-3 and envelop coding pHXB2 plasmids were co-transfected in HEK293T using a calcium phosphate method. Virus-containing culture supernatants were collected after 48 h of transfection, clarified by centrifugation at 300 × *g* for about 5 min and passed through filters of 0.45 μm pores. The quantification of retroviral reverse transcriptase activity in a retrovirus containing supernatant by quantitative reverse transcription PCR as a method for titration of the lentiviral/retrovirus vector was followed.[33,34] The virus was five-fold diluted, and TZM GFP cells were infected for 48 h. Green cells, as well as total cells, were scored using the SpectraMax i3x platform, and the percentage infectivity was represented in a graph. To check the cell number after incubating with the frameworks for 48 h, cells were fixed with Hoechst and counted in the Thermo HCS platform and represented in bar plots.

Conflicts of interest

The authors declare the following competing financial interest. A patent application has been filed on ''Metal chelated nanoporous organic frameworks'' with A. Patra, A. Chande, MD. W. Hussain and V. Bhardwaj as inventors.

Acknowledgements

Financial support from DST/CHM/2018/086 [DST/TM/WTI/WIC/2K17/82(G)] and SERB/CHM/2017/113 (file no. EMR/2017/000233), infrastructural support from IISERB, and the FIST supported TEM facility to the Dept. of Chemistry, IISERB are gratefully acknowledged. AC thanks the IYBA fellowship (BT/010/IYBA/2017/01) and a grant (BT/PR26013/GET/119/191/2017) from the Department of Biotechnology, Government of India for generous funding. VB is supported by a fellowship from CSIR; WH and AG acknowledge UGC for fellowship. The authors thank Massimo Pizzato, Jeremy Luban, and the NIH AIDS Reagent Program for providing the reagents, plasmids, and cell lines. psPAX2 and pMD2.G plasmids were a gift from Didier Trono.

Notes and references

1 (*a*) S. Solomon, G. K. Plattner, R. Knutti and P. Friedlingstein, *Proc. Natl. Acad. Sci., U. S. A.*, 2009, **106**, 1704; (*b*) L. Zou, Y. Sun, S. Che, X. Yang, X. Wang, M. Bosch, Q. Wang, H. Li, M. Smith, S. Yuan, Z. Perry and H. Zhou, *Adv. Mater.*, 2017, **29**, 1700229.

2 (*a*) A. Muñoz-Bonilla and M. Fernández-García, *Prog. Polym. Sci.*, 2012, **37**, 281; (*b*) V. B. Schwartz, F. Thétiot, S. Ritz, S. Pütz, L. Choritz, A. Lappas, R. Förch, K. Landfester and U. Jonas, *Adv. Funct. Mater.*, 2012, **22**, 2376; (*c*) Y. Yuan, F. Sun, F. Zhang, H. Ren, M. Guo, K. Cai, X. Jing, X. Gao and G. Zhu, *Adv. Mater.*, 2013, **25**, 6619.

3 (*a*) G. Ji, Z. Yang, H. Zhang, Y. Zhao, B. Yu, Z. Ma and Z. Liu, *Angew. Chem., Int. Ed.*, 2016, **55**, 9685; (*b*) Y. Yuan and G. Zhu, *ACS Cent. Sci.*, 2019, **5**, 409.

4 (*a*) S. Bandyopadhyay, A. G. Anil, A. James and A. Patra, *ACS Appl. Mater. Interfaces*, 2016, **8**, 27669; (*b*) J. Wu, F. Xu, S. Li, P. Ma, X. Zhang, Q. Liu, R. Fu and D. Wu, *Adv. Mater.*, 2019, **31**, 1802922.

5 (*a*) S. Choi, J. H. Drese and C. W. Jones, *ChemSusChem*, 2009, **2**, 796; (*b*) A. G. Slater and A. I. Cooper, *Science*, 2015, **348**, aaa8075; (*c*) M. Ding, R. W. Flaig, H. L. Jiang and O. M. Yaghi, *Chem. Soc. Rev.*, 2019, **48**, 2783.

6 (*a*) T. Sakakura and K. Kohno, *Chem. Commun.*, 2009, 1312; (*b*) C. Martín, G. Fiorani and A. W. Kleij, *ACS Catal.*, 2015, **5**, 1353; (*c*) X. Wang, Y. Zhou, Z. Guo, G. Chen, J. Li, Y. Shi, Y. Liu and J. Wang, *Chem. Sci.*, 2015, **6**, 6916.

7 (*a*) P. Kaur, J. T. Hupp and S. T. Nguyen, *ACS Catal.*, 2011, **1**, 819; (*b*) K. Huang, J. Y. Zhang, F. J. Liu and S. Dai, *ACS Catal.*, 2018, **8**, 9079; (*c*) A. Giri, M. W. Hussain, B. Sk and A. Patra, *Chem. Mater.*, 2019, **31**, 8440.

8 (*a*) A. Thomas, *Angew. Chem., Int. Ed.*, 2010, **49**, 8328; (*b*) D. Wu, F. Xu, B. Sun, R. W. Fu, H. K. He and K. Matyjaszewski, *Chem. Rev.*, 2012, **112**, 3959; (*c*) A. Patra and U. Scherf, *Chem.–Eur. J.*, 2012, **18**, 10074; (*d*) H. Urakami, K. Zhang and F. Vilela, *Chem. Commun.*, 2013, **49**, 2353; (*e*) T. Islamoglu, M. G. Rabbani and H. M. El-Kaderi, *J. Mater. Chem. A*, 2013, **1**, 10259; (*f*) Y. H. Xu, S. B. Jin, H. Xu, A. Nagai and D. Jiang, *Chem. Soc. Rev.*, 2013, **42**, 8012; (*g*) N. Chaoui, M. Trunk, R. Dawson, J. Schmidt and A. Thomas, *Chem. Soc. Rev.*, 2017, **46**, 3302; (*h*) H. A. Patel, J. Byun and C. T. Yavuz, *ChemSusChem*, 2017, **10**, 1303; (*i*) A. Khayum M, M. Ghosh, V. Vijayakumar, A. Halder, M. Nurhuda, S. Kumar, M. Addicoat, S. Kurungot and R. Banerjee, *Chem. Sci.*, 2019, **10**, 8889.

9 (*a*) X. Q. Zou, H. Ren and G. Zhu, *Chem. Commun.*, 2013, **49**, 3925; (*b*) J. Luo, X. Zhang, J. Z. Lu and J. Zhang, *ACS Catal.*, 2017, **7**, 5062.

10 (*a*) O. Buyukcakir, S. H. Je, D. S. Choi, S. N. Talapaneni, Y. Seo, Y. Jung, K. Polychronopoulou and A. Coskun, *Chem. Commun.*, 2016, **52**, 934; (*b*) D. Xu, J. N. Guo and F. Yan, *Prog. Polym. Sci.*, 2018, **79**, 121; (*c*) R. Luo, X. Liu, M. Chen, B. Liu and Y. Fang, *ChemSusChem*, 2020, DOI: 10.1002/cssc.202001079.

11 (*a*) Y. Zhang, J. Jiang and Y. Chen, *Polymer*, 1999, **40**, 6189; (*b*) A. C. Engler, N. Wiradharma, Z. Y. Ong, D. J. Coady, J. L. Hedrick and Y. Y. Yang, *Nano Today*, 2012, **7**, 201; (*c*) J. Budhathoki-Uprety, L. Peng, C. Melander and B. M. Novak, *ACS Macro Lett.*, 2012, **1**, 370.

12 S. Mitra, S. Kandambeth, B. P. Biswal, M. A. Khayum, C. K. Choudhury, M. Mehta, G. Kaur, S. Banerjee, A. Prabhune, S. Verma, S. Roy, U. K. Kharul and R. Banerjee, *J. Am. Chem. Soc.*, 2016, **138**, 2823.

13 (*a*) Q. Sun, B. Aguila, J. Perman, N. Nguyen and S. Ma, *J. Am. Chem. Soc.*, 2016, **138**, 15790; (*b*) Y. Du, H. S. Yang, S. Wan, Y. H. Jin and W. Zhang, *J. Mater. Chem. A*, 2017, **5**, 9163; (*c*) S. Kramer, N. R. Bennedsen and S. Kegnaes, *ACS Catal.*, 2018, **8**, 6961; (*d*) L. P. Jing, J. S. Sun, F. Sun, P. Chen and G. Zhu, *Chem. Sci.*, 2018, **9**, 3523; (*e*) Y. Zhang, P. Sun, L. Zhang, Z. Wang, F. Wang, K. Dong, Z. Liu, J. Ren and X. Qu, *Adv. Funct. Mater.*, 2019, **29**, 1808594.

14 O. Buyukcakir, S. H. Je, S. N. Talapaneni, D. Kim and A. Coskun, *ACS Appl. Mater. Interfaces*, 2017, **9**, 7209.

15 (*a*) P. Mwimanzi, I. Tietjen, S. C. Miller, A. Shahid, K. Cobarrubias, N. N. Kinloch, B. Baraki, J. Richard, A. Finzi, D. Fedida, Z. L. Brumme and M. A. Brockman, *J. Virol.*, 2016, **90**, 9495; (*b*) J. Francos and V. Cadierno, *Dalton Trans.*, 2019, **48**, 9021.

16 (*a*) X. Deng, Q. Luan, W. Chen, Y. Wang, M. Wu, H. Zhang and Z. Jiao, *Nanotechnology*, 2009, **20**, 115101; (*b*) W. Song, J. Zhang, J. Guo, J. Zhang, F. Ding, L. Li and Z. Sun, *Toxicol. Lett.*, 2010, **199**, 389–397; (*c*) A. Sirelkhatim, S. Mahmud, A. Seeni, N. H. M. Kaus, L. C. Ann, S. K. M. Bakhori, H. Hasan and D. Mohamad, *Nano-Micro Lett.*, 2015, **7**, 219.

17 (*a*) S. Lee, S. Jeong, D. Kim, S. Hwang, M. Jeon and J. Moon, *Superlattices Microstruct.*, 2008, **43**, 330; (*b*) M. Wang, A. D. Li, J. Z. Kong, Y. P. Gong, C. Zhao, Y. F. Tang and D. Wu, *Nanoscale Res. Lett.*, 2018, **13**, 47; (*c*) P. Ingale, K. Knemeyer, M. P. Hermida, R. N. d'Alnoncourt, A. Thomas and F. Rosowski, *Nanomaterials*, 2020, **10**, 981.

18 G. Das, S. Nagaraja, V. Sridurai, D. B. Shinde, M. Addicoat, T. Prakasam, F. Gándara, F. Ravaux, S. K. Sharma, G. G. Nair, Z. Lai, R. Jagannathan, M. A. Olson and A. Trabolsi, *Chem. Mater.*, 2019, **31**, 4148.

19 E. Castillejos-López, G. Agostini, M. D. Michel, A. Iglesias-Juez and B. Bachiller-Baeza, *ACS Catal.*, 2017, **7**, 796.

20 (*a*) D. Gu and F. Schüth, *Chem. Soc. Rev.*, 2014, **43**, 313; (*b*) M. Thommes, K. Kaneko, A. V. Neimark, J. P. Olivier, F. Rodriguez-Reinoso, J. Rouquerol and K. S. W. Sing, *Pure Appl. Chem.*, 2015, **87**, 1051.

21 (*a*) W. G. Lu, J. P. Sculley, D. Q. Yuan, R. Krishna, Z. W. Wei and H. Zhou, *Angew. Chem., Int. Ed.*, 2012, **51**, 7480; (*b*) R. Dawson, A. I. Cooper and D. J. Adams, *Polym. Int.*, 2013, **62**, 345; (*c*) Y. Zhu and W. Zhang, *Chem. Sci.*, 2014, **5**, 4957; (*d*) T. Jin, Y. Xiong, X. Zhu, Z. Tian, D. J. Tao, J. Hu, D. Jiang, H. Wang, H. Liu and S. Dai, *Chem. Commun.*, 2016, **52**, 4454; (*e*) M. W. Hussain, S. Bandyopadhyay and A. Patra, *Chem. Commun.*, 2017, **53**, 10576; (*f*) H. G. Wang, Z. H. Cheng, Y. Z. Liao, J. H. Li, J. Weber, A. Thomas and C. F. J. Faul, *Chem. Mater.*, 2017, **29**, 4885.

22 M. W. Hussain, A. Giri and A. Patra, *Sustainable Energy Fuels*, 2019, **3**, 2567.

23 (*a*) A. Tavakoli, A. Ataei-Pirkooh, G. M. Sadeghi, F. Bokharaei-Salim, P. Sahrapour, S. J. Kiani, M. Moghoofei, M. Farahmand, D. Javanmard and S. H. Monavari, *Nanomedicine*, 2018, **13**, 2675; (*b*) H. Ghaffari, A. Tavakoli, A. Moradi, A. Tabarraei, F. Bokharaei-Salim, M. Zahmatkeshan, M. Farahmand, D. Javanmard, S. J. Kiani, M. Esghaei, V. Pirhajati-Mahabadi, S. H. Monavari and A. A. Pirkooh, *J. Biomed. Sci.*, 2019, **26**, 70.

24 S. Pal, Y. K. Tak and J. M. Song, *Appl. Environ. Microbiol.*, 2007, **73**, 1712.

25 S. N. Rampersad, *Sensors*, 2012, **12**, 12347.

26 H. Bai, H. Yuan, C. Nie, B. Wang, F. Lv, L. Liu and S. Wang, *Angew. Chem., Int. Ed.*, 2015, **54**, 13208.

27 (*a*) H. Flemming, J. Wingender, U. Szewzyk, P. Steinberg, S. A. Rice and S. Kjelleberg, *Nat. Rev. Microbiol.*, 2016, **14**, 563; (*b*) C. C. C. R. de Carvalho, *Front. Mar. Sci.*, 2018, **5**, 126.

28 (*a*) L. A. T. W. Asri, M. Crismaru, S. Roest, Y. Chen, O. Ivashenko, P. Rudolf, J. C. Tiller, H. C. van der Mei, T. J. A. Loontjens and H. J. Busscher, *Adv. Funct. Mater.*, 2014, **24**, 346; (*b*) P. Zhang, S. Li, H. Chen, X. Wang, L. Liu, F. Lv and S. Wang, *ACS Appl. Mater. Interfaces*, 2017, **9**, 16933; (*c*) X. Li, B. Wu, H. Chen, K. Nan, Y. Jin, L. Suna and B. Wang, *J. Mater. Chem. B*, 2018, **6**, 4274; (*d*) M. Hu, K. Korschelt, M. Viel, N. Wiesmann, M. Kappl, J. Brieger, K. Landfester, H. Therien-Aubin and W. Tremel, *ACS Appl. Mater. Interfaces*, 2018, **10**, 44722; (*e*) Z. Li, X. Feng, S. Gao, Y. Jin, W. Zhao, H. Liu, X. Yang, S. Hu, K. Cheng and J. Zhang, *ACS Appl. Bio Mater.*, 2019, **2**, 613; (*f*) A. Panjla, G. Kaul, M. Shukla, S. Tripathi, N. N. Nair, S. Chopra and S. Verma, *Chem. Commun.*, 2019, **55**, 8599.

29 G. Grégori, S. Citterio, A. Ghiani, M. Labra, S. Sgorbati, S. Brown and M. Denis, *Appl. Environ. Microbiol.*, 2001, **67**, 4662.

30 D. Y. Sasaki and T. M. Alam, *Chem. Mater.*, 2000, **12**, 1400.

31 A. Rosa, A. Chande, S. Ziglio, V. De Sanctis, R. Bertorelli, S. L. Goh, S. M. McCauley, A. Nowosielska, S. E. Antonarakis, J. Luban, F. A. Santoni and M. Pizzato, *Nature*, 2015, **526**, 212.

32 A. Chande, E. C. Cuccurullo, A. Rosa, S. Ziglio, S. Carpenter and M. Pizzato, *Proc. Natl. Acad. Sci. U. S. A.*, 2016, **113**, 13197.

33 M. Pizzato, O. Erlwein, D. Bonsall, S. Kaye, D. Muir and M. O. McClure, *J. Virol. Methods*, 2009, **156**, 1.

34 J. Vermeire, E. Naessens, H. Vanderstraeten, A. Landi, V. Iannucci, A. Van Nuffel, T. Taghon, M. Pizzato and B. Verhasselt, *PLoS One*, 2012, **7**, e50859.

35 V. Cagno, P. Andreozzi, M. D'Alicarnasso, P. Jacob Silva, M. Mueller, M. Galloux, R. Le Goffic, S. T. Jones, M. Vallino, J. Hodek, J. Weber, S. Sen, E. R. Janeček, A. Bekdemir, B. Sanavio, C. Martinelli, M. Donalisio, M. A. R. Welti, J. F. Eleouet, Y. Han, L. Kaiser, L. Vukovic, C. Tapparel, P. Král, S. Krol, D. Lembo and F. Stellacci, *Nat. Mater.*, 2017, **17**, 195.

36 B. Shogan, L. Kruse, G. B. Mulamba, A. Hu and D. M. Coen, *J. Virol.*, 2006, **80**, 4740.

37 P. Pallavi, V. Kumar, M. W. Hussain and A. Patra, *ACS Appl. Mater. Interfaces*, 2018, **10**, 44696.

38 (*a*) A. L. Koch, *Anal. Biochem.*, 1970, **38**, 252; (*b*) B. D. Jett, K. L. Hatter, M. M. Huycke and M. S. Gilmore, *BioTechniques*, 1997, **23**, 648.